

Kinetic Understanding of Catalytic Selectivity and Product Distribution of Electrocatalytic Carbon Dioxide Reduction Reaction

Dai-Jian Su^{a#}, Shi-Qin Xiang^{a#}, Shu-Ting Gao^a, Yimin Jiang^a, Xiaohong Liu^b, Wei Zhang^{b*}, Liu-Bin Zhao^{a*}, and Zhong-Qun Tian^c

^aDepartment of Chemistry, School of Chemistry and Chemical Engineering, Southwest University, Chongqing, 400715, China

^bChongqing Institute of Green and Intelligent Technology, Chinese Academy of Sciences, Chongqing, 400714, China

^cState Key Laboratory for Physical Chemistry of Solid Surfaces, College of Chemistry and Chemical Engineering, Collaborative Innovation Center of Chemistry for Energy Materials, Xiamen University, Xiamen 361005, China

*Email: lbzhao@swu.edu.cn; zhangwei@cigit.ac.cn

[#]Dai-Jian Su and Shi-Qin Xiang contributed equally to this paper

Table of Contents

1. Micro-kinetic model	3
1.1 Derivation of activation barrier Energy based on Marcus theory.....	3
1.2 Computation of reorganization energies.....	4
1.3 Heterogenous charge transfer rate constant.....	5
Table S1	6
Table S2	7
2. Adsorption configurations	8
Table S3	8
3. Reaction thermodynamics vs. kinetics	10
Scheme S1	10
Scheme S2	11
Table S4.....	12
Figure S1.....	15
Table S6.....	16
Table S7.....	17
4. Potential energy curves.....	18
Figure S2.....	18
5. Activation barriers and rate constants.....	19
Figure S3.....	19
Figure S4.....	20
Table S8	21
6. Faradaic efficiencies	23
Figure S5.....	23
7. Hydrogen evolution reaction	25
Table S9.....	26
Table S10.....	27
Figure S6.....	28
Figure S7.....	29
8. References.....	30

1. Micro-kinetic model

1.1 Derivation of activation barrier Energy based on Marcus theory

According to our previous work, the activation energy barrier E_a is derived based on Marcus theory,¹⁻² and the specific process is as follows:

For a displaced oscillator model, free energy of transition state is expressed as

$$E_R = \frac{1}{2} kx^2 \rightarrow x^2 = \frac{2E_R}{k} \quad (1)$$

$$E_P = \frac{1}{2} k(x-q)^2 + \Delta G \quad (2)$$

Where k is force constants of reactant systems and product systems, respectively; G is reaction free energy; q is the reaction coordinates. We defined $\lambda = (1/2)kq^2$, then

$$E_R = E_P = E_a = \frac{\lambda}{4} \left(1 + \frac{\Delta G}{\lambda}\right)^2 \quad (3)$$

For a displaced-distorted oscillator model, free energy of transition state is expressed as

$$E_R = \frac{1}{2} k_R x^2 \rightarrow x^2 = \frac{2E_R}{k_R} \quad (4)$$

$$E_P = \frac{1}{2} k_P (x-q)^2 + \Delta G \quad (5)$$

Where k_R and k_P is force constants of reactant systems and product systems, respectively; ΔG is reaction free energy; q is the reaction coordinates. We defined

$$\lambda_R = \frac{1}{2} k_R q^2, \lambda_P = \frac{1}{2} k_P q^2 \quad (6)$$

Where λ_R is the total reorganization energy of reactant systems, λ_P is the total reorganization energy of product systems.

Then, the reaction barrier E_a can be computed from the reaction free energy and reorganization energies.³⁻⁵

$$E_a = \left(\frac{-\sqrt{\lambda_R} + \sqrt{\frac{\lambda_R}{\lambda_P} \left[\lambda_R + \Delta G \left(\frac{\lambda_R}{\lambda_P} - 1 \right) \right]}}{\left(\frac{\lambda_R}{\lambda_P} - 1 \right)} \right)^2 \quad (7)$$

Here ΔG is the free energy change, and λ_R and λ_P represent the total reorganization energy of reactant and product.

1.2 Computation of reorganization energies

The total reorganization energy consists of three parts, including internal reorganization energy ($\lambda_{R/P}^i$), electron transfer solvent reorganization energy ($\lambda_{R/P}^{o,ET}$) and proton transfer solvent reorganization energy ($\lambda_{R/P}^{o,PT}$).

$$\lambda_{R/P} = \lambda_{R/P}^i + \lambda_{R/P}^{o,ET} + \lambda_{R/P}^{o,PT} \quad (8)$$

The inner reorganization energies defined as electronic energy difference along the general reaction coordinate from the equilibrium configuration of reactant to the equilibrium configuration of product.

$$\lambda_R^i = E_R(P_e) - E_R(R_e) \quad (9)$$

$$\lambda_P^i = E_P(P_e) - E_P(R_e) \quad (10)$$

Where $E_R(R_e)$ and $E_P(P_e)$ are electronic energy of the reactant and product in their equilibrium configurations, respectively. $E_R(P_e)$ denotes single point energy of reactant under the equilibrium configuration of the product and $E_P(R_e)$ denotes single point energy of product under the equilibrium configuration of the reactant. To keep the conservation of matter, one hydrogen atom is removed from the product in single point energy calculation of $E_R(P_e)$, while one hydrogen atom is added to the reactant in single point energy calculation of $E_P(R_e)$.

The outer (solvent) reorganization energies are obtained from polarization continuum electrostatic model.⁶⁻⁷

$$\lambda_{R/P}^{o,ET} = \frac{e^2}{4\pi\epsilon_0} \left(\frac{1}{\epsilon_{op}} - \frac{1}{\epsilon_s} \right) \frac{1}{2a} \quad (11)$$

$$\lambda_{R/P}^{o,PT} = \frac{1}{4\pi\epsilon_0} \left(\frac{\epsilon_s - 1}{2\epsilon_s + 1} - \frac{\epsilon_{op} - 1}{2\epsilon_{op} + 1} \right) \frac{(\mu_R - \mu_P)^2}{a^3} \quad (12)$$

1.3 Heterogenous charge transfer rate constant

Heterogenous charge transfer rate constants are calculated by Marcus-Gerischer theory⁸⁻⁹ which accounts for sum of the partial electron transition probabilities between the redox level at energy ε_r and the electron states with energy ε_k in the electrode. The energy difference between ε_r and the electron states with energy ε_k at Fermi level is assumed to be the reaction free energy ΔG . The integration over all energy states ε in electrode provides the total rate constant,

$$k = \frac{k_B T}{h} \int_{-\infty}^{+\infty} \rho(\varepsilon) f(\varepsilon) \exp\left(-\frac{E_a(\varepsilon)}{k_B T}\right) d\varepsilon \quad (13)$$

Where $f(\varepsilon)$ is the Fermi-Dirac distribution and $\rho(\varepsilon)$ is the density of states in the electrode that can be obtained from electronic structure computations.

$$f(\varepsilon) = \left[1 + \exp\left(\frac{\varepsilon - \varepsilon_F}{k_B T}\right) \right]^{-1} \quad (14)$$

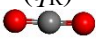

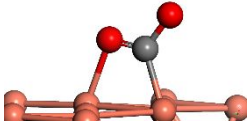
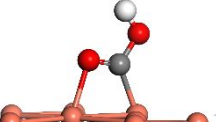
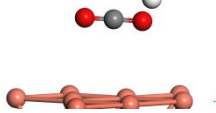
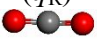

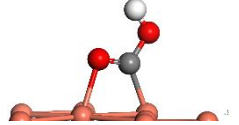
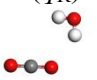

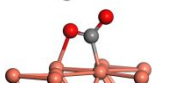
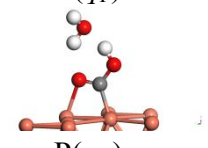
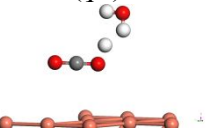
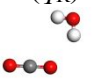
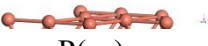
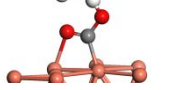
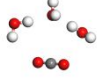
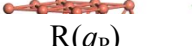
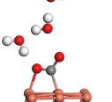
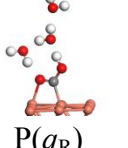
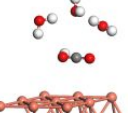

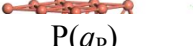
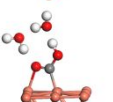
The activation energies for the multiple potential energy curve case in different range of ε_k is given by¹⁰⁻¹¹

(i) $E_a = \Delta G$ for barrierless charge transfer region (symmetry factor $\beta = 1$) where $\Delta G \geq \lambda_R$.

(ii) Equation (7) where E_a varies as a function of ΔG and λ for normal charge transfer region (symmetry factor $0 < \beta < 1$) where $-\lambda_p < \Delta G < \lambda_R$.

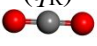

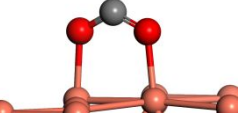
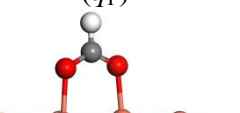
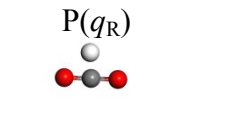

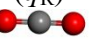
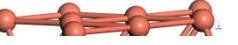
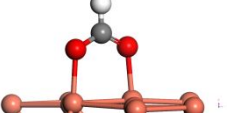
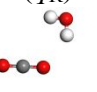
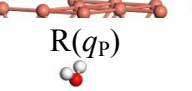
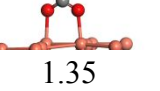
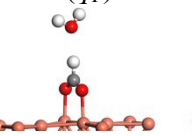
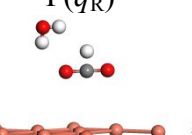
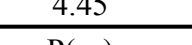
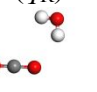
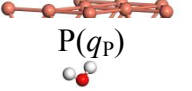
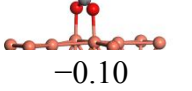
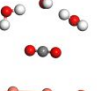
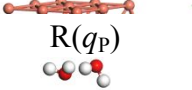
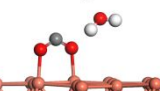
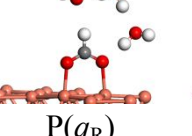
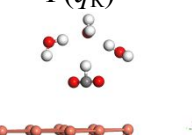
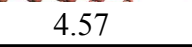
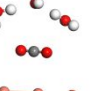
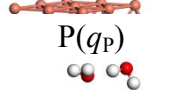
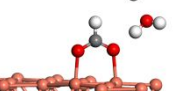
(iii) $E_a = 0$ for activationless charge transfer region (symmetry factor $\beta = 0$) where $\Delta G \leq -\lambda_p$.

Table S1. Comparison of calculated inner reorganization energies λ^i (eV) and reaction free energies ΔG (eV) for $^*\text{CO}_2 + \text{H}^+ + \text{e}^- \rightarrow ^*\text{COOH}$ on Cu(111) surface with different number of explicit water molecules.

	λ_{R}^i (eV)	λ_{P}^i (eV)	ΔG (eV)
Without H ₂ O	$\text{R}(q_{\text{R}})$   $\text{R}(q_{\text{P}})$  1.17	$\text{P}(q_{\text{P}})$  $\text{P}(q_{\text{R}})$  1.72	$\text{R}(q_{\text{R}})$   $\text{P}(q_{\text{P}})$  0.60
With 1H ₂ O	$\text{R}(q_{\text{R}})$   $\text{R}(q_{\text{P}})$  1.32	$\text{P}(q_{\text{P}})$  $\text{P}(q_{\text{R}})$  1.88	$\text{R}(q_{\text{R}})$   $\text{P}(q_{\text{P}})$  0.48
With 3H ₂ O	$\text{R}(q_{\text{R}})$   $\text{R}(q_{\text{P}})$  1.38	$\text{P}(q_{\text{P}})$  $\text{P}(q_{\text{R}})$  2.35	$\text{R}(q_{\text{R}})$   $\text{P}(q_{\text{P}})$  0.36

As derived in Equation 3, the computed activation barriers vary as a function of ΔG (reaction driving force) and λ (reaction resistance) values. The uncertainty (error) of reaction barriers should thus arise from the calculated ΔG and λ values. DFT calculation results presented in the main text are performed by using implicit polarizable continuum model. In order to test the influence of short-range solvation effect of explicit solvent molecules, DFT calculations of competing COOH* and HCOO* formation on Cu(111) surface with and without explicit water molecules are compared in Table S1 and S2.

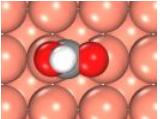
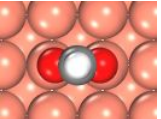
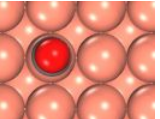
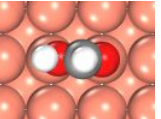
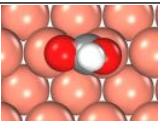
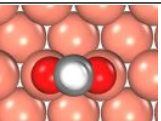
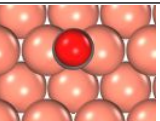
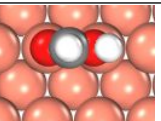
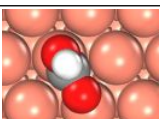
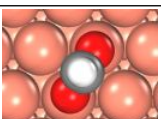
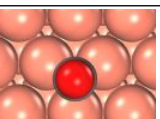
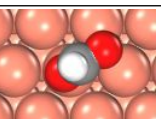
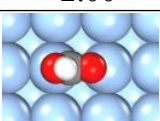
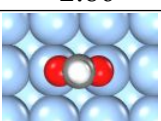
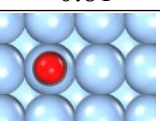
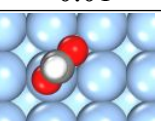
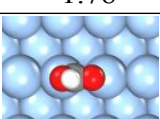
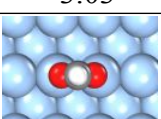
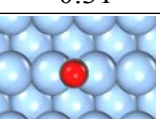
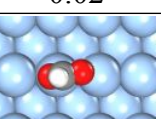
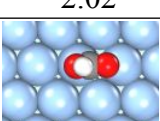
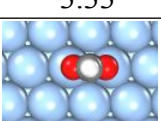
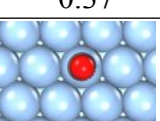
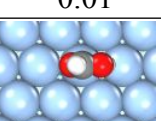
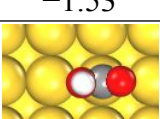
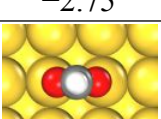
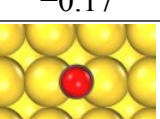
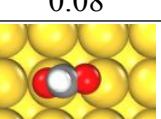
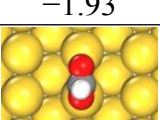
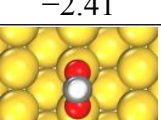
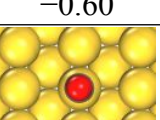
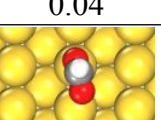
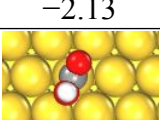
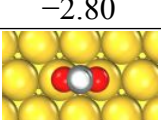
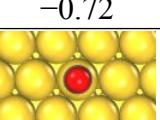
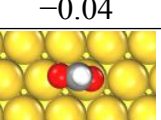
Table S2. Comparison of calculated inner reorganization energies λ^i (eV) and reaction free energies ΔG (eV) for $^*\text{CO}_2 + \text{H}^+ + \text{e}^- \rightarrow ^*\text{HCOO}$ on Cu(111) surface with different number of explicit water molecules.

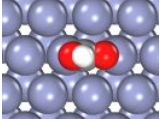
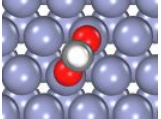
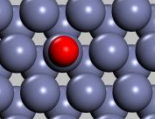
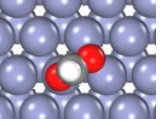
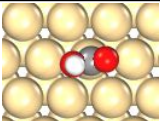
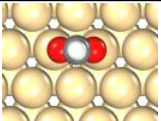
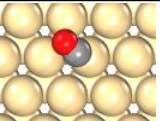
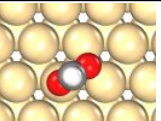
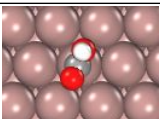
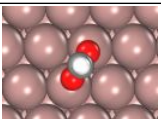
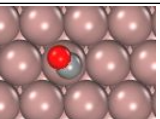
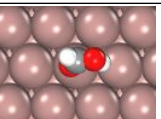
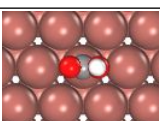
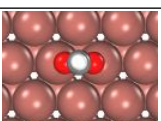
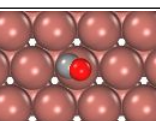
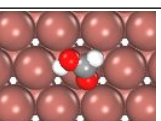
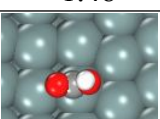
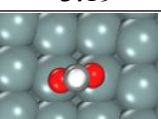
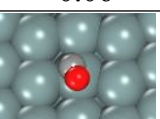
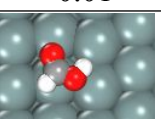
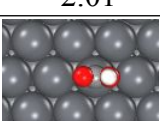
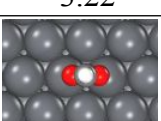
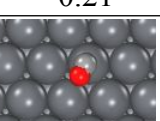
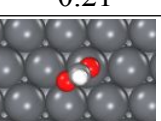
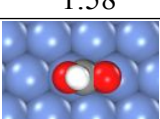
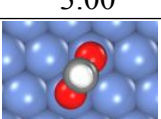
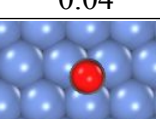
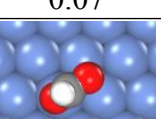
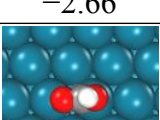
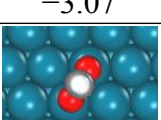
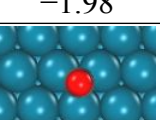
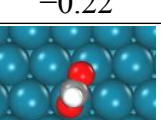
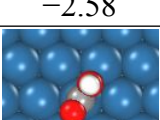
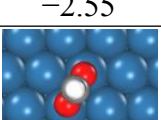
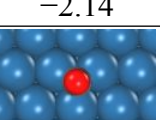
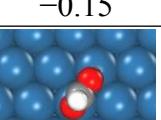
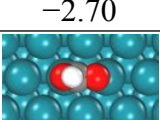
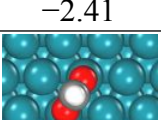
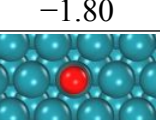
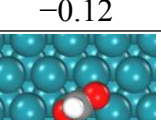
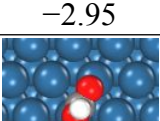
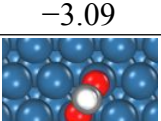
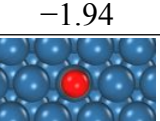
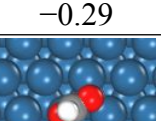
	λ_{R}^i (eV)	λ_{P}^i (eV)	ΔG (eV)
Without H ₂ O	$\text{R}(q_{\text{R}})$   $\text{R}(q_{\text{P}})$  1.33	$\text{P}(q_{\text{P}})$  $\text{P}(q_{\text{R}})$   4.55	$\text{R}(q_{\text{R}})$   $\text{P}(q_{\text{P}})$  -0.03
With 1H ₂ O	$\text{R}(q_{\text{R}})$   $\text{R}(q_{\text{P}})$  1.35	$\text{P}(q_{\text{P}})$  $\text{P}(q_{\text{R}})$   4.45	$\text{R}(q_{\text{R}})$   $\text{P}(q_{\text{P}})$  -0.10
With 3H ₂ O	$\text{R}(q_{\text{R}})$   $\text{R}(q_{\text{P}})$  1.30	$\text{P}(q_{\text{P}})$  $\text{P}(q_{\text{R}})$   4.57	$\text{R}(q_{\text{R}})$   $\text{P}(q_{\text{P}})$  -0.19

It is shown that the presence of water molecules has quite weak influence on the calculated ΔG and λ , and the energy difference between derived activation barriers with and without explicit water molecules is less than 0.12 (0.06) eV for COOH* (HCOO) formation.

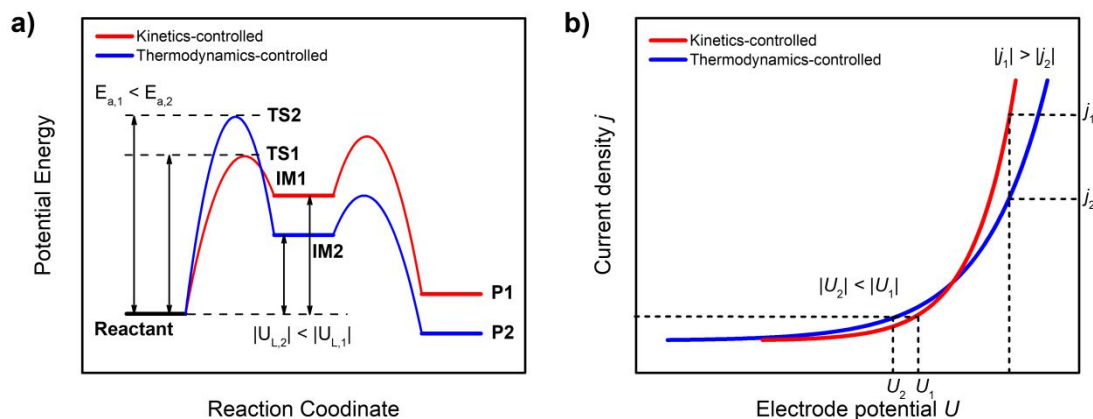
2. Adsorption configurations

Table S3. Adsorption configurations and binding energies (in eV) of COOH, HCOO, CO, and HCOOH on various metal surfaces.

Surfaces	COOH	HCOO	CO	HCOOH
Cu(100)	 -2.28	 -3.35	 -0.92	 -0.16
Cu(110)	 -2.47	 -3.67	 -0.94	 -0.33
Cu(111)	 -2.00	 -2.86	 -0.81	 -0.01
Ag(100)	 -1.78	 -3.03	 -0.31	 0.02
Ag(110)	 -2.02	 -3.33	 -0.37	 -0.01
Ag(111)	 -1.53	 -2.75	 -0.17	 0.08
Au(100)	 -1.93	 -2.41	 -0.60	 0.04
Au(110)	 -2.13	 -2.80	 -0.72	 -0.04
Au(111)	 -1.78	 -2.25	 -0.31	 0.09

Zn(001)	 -1.88	 -3.14	 0.04	 0.09
Cd(001)	 -1.91	 -3.23	 -0.08	 0.02
In(101)	 -1.75	 -3.29	 -0.05	 0.02
Tl(001)	 -1.48	 -3.19	 -0.06	 -0.01
Sn(100)	 -2.01	 -3.22	 -0.21	 -0.21
Pb(111)	 -1.58	 -3.00	 -0.04	 0.07
Ni(111)	 -2.66	 -3.07	 -1.98	 -0.22
Pd(111)	 -2.58	 -2.55	 -2.14	 -0.15
Pt(111)	 -2.70	 -2.41	 -1.80	 -0.12
Rh(111)	 -2.95	 -3.09	 -1.94	 -0.29
Ir(111)	 -2.96	 -2.98	 -1.98	 -0.21

3. Reaction thermodynamics vs. kinetics

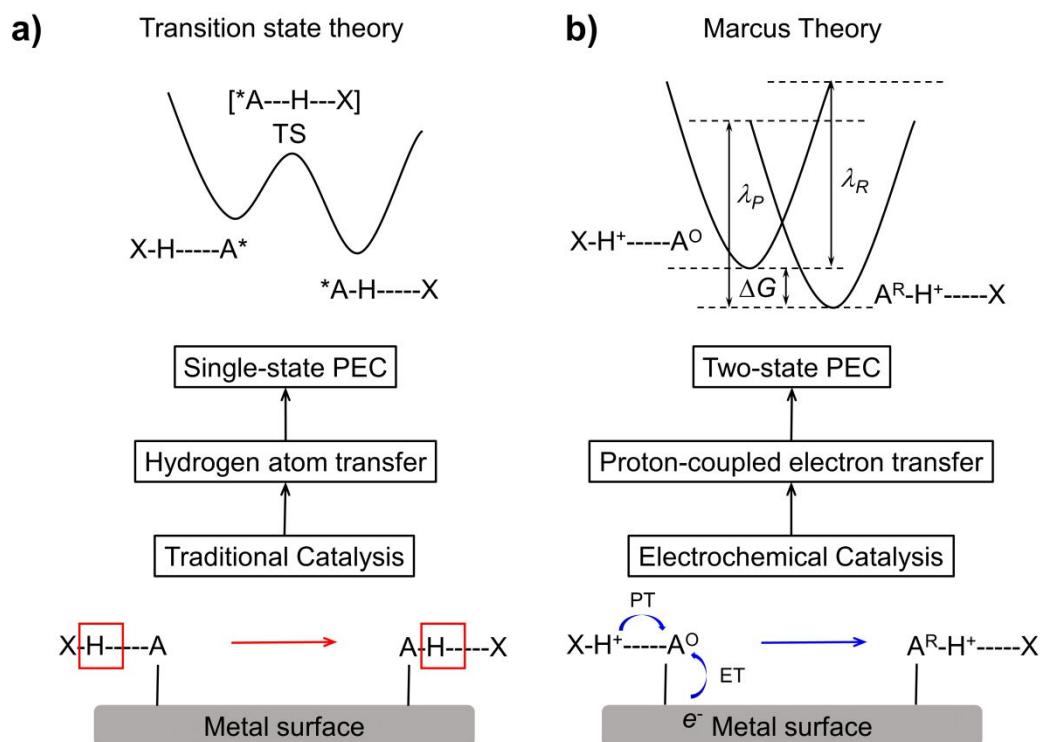


Scheme S1. Comparison of (a) potential energy curves and (b) polarization curves of kinetics-controlled and thermodynamic-controlled parallel reactions.

Scheme S1a compares the potential energy curves of parallel reaction of the same reactant to different products P1 and P2, in which the product selectivity predicted by kinetic computation is just opposite to that by thermodynamic calculations. P1 is a thermodynamics-controlled product because of lower onset potential, while P2 is a kinetics-controlled product due to smaller reaction activation barrier.

To make a direct comparison with experimental results, the calculated potential energy curves need to convert to current-potential relations.

Scheme S1b compares the polarization curves for competing generation of P1 and P2. Because thermodynamics-controlled P2 is produced ahead of P1, the overpotential of P2 is lower than that of P1 within small current density. As the increase of potential polarization, the current density of kinetics-controlled P1 rapidly surpasses that of P2 at higher overpotential. In next section, the catalytic selectivities of CO₂ reduction to CO and FA will be discussed within electrochemical micro-kinetics model.



Scheme S2. Comparison of reaction barrier of a proton-coupled electron transfer reaction calculated by (a) transition state theory and (b) Marcus charge transfer theory.

In previous kinetic studies on CO₂RR, the electrochemical proton-electron transfer reactions were usually treated as hydrogen atom transfer reactions. The reaction barriers were determined by searching the transition states along single-state potential energy curves of elementary hydrogenation steps. However, the hydrogen atom transfer model cannot well reflect the realistic electrode processes, in which electrons are transferred from the electrode while the protons are transferred from electrolyte. In this work, the potential-dependent electrochemical rate constants are obtained using micro-kinetic model based on Marcus theory that can directly compared with electrochemical experimental measurements.

Table S4. Reaction Barrier (in eV) of CO₂RR Calculated by CI-NEB Method and Marcus Charge Transfer Theory.

Metal	CO ₂ * + H* → COOH*		CO ₂ * + H ⁺ + e ⁻ → COOH*	
	$U = U_{H^*}$	$U = U_{SHE}$	$U = U_{H^*}$	$U = U_{SHE}$
Cu(111)	0.92	0.97	0.93	0.99
)				
Au(111)	0.48	0.73	0.66	1.00
)				
In(101)	1.21	1.64	0.64	1.07
Metal	CO ₂ * + H* → HCOO*		CO ₂ * + H ⁺ + e ⁻ → HCOO*	
	$U = U_{H^*}$	$U = U_{SHE}$	$U = U_{H^*}$	$U = U_{SHE}$
Cu(111)	0.76	0.81	0.87	0.91
)				
Au(111)	0.81	1.05	1.08	1.32
)				
In(101)	-0.45	-0.02	0.49	0.74
Metal	COOH* + H* → CO* + H ₂ O		COOH* + H ⁺ + e ⁻ → CO* + H ₂ O	
	$U = U_{H^*}$	$U = U_{SHE}$	$U = U_{H^*}$	$U = U_{SHE}$
Cu(111)	1.11	1.16	0.37	0.41
)				
Au(111)	0.08	0.32	0.23	0.44
)				
In(101)	0.01	0.44	0.29	0.62
Metal	HCOO* + H* → HCOOH*		HCOO* + H ⁺ + e ⁻ → HCOOH*	
	$U = U_{H^*}$	$U = U_{SHE}$	$U = U_{H^*}$	$U = U_{SHE}$
Cu(111)	0.51	0.56	0.52	0.58
)				
Au(111)	0.38	0.62	0.12	0.29
)				
In(101)	0.15	0.58	0.38	0.86

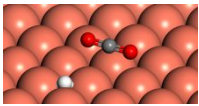
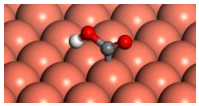
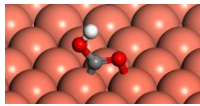
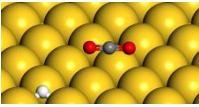
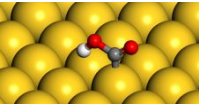
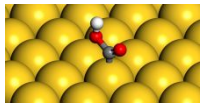
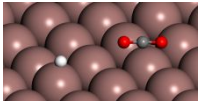
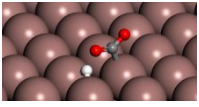
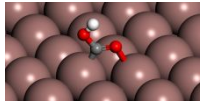
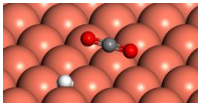
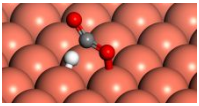
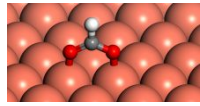
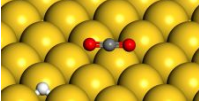
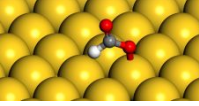
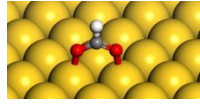
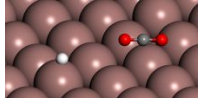
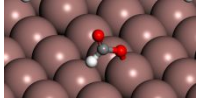
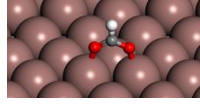
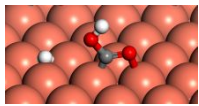
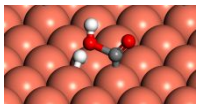
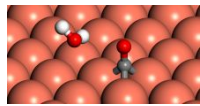
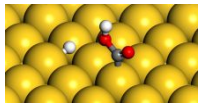
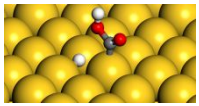
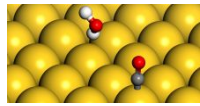
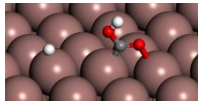
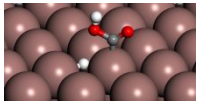
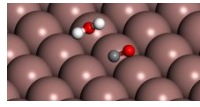
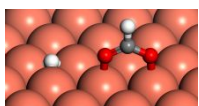
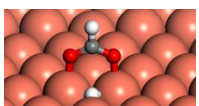
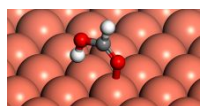
U_{SHE} is defined as $U = 0$ V vs. SHE

U_{H^*} is defined as the electrode potential at which the formation free energy of H* is zero. $U_{H^*} = -0.10$ V on Cu(111), $U_{H^*} = -0.49$ V on Au(111), and $U_{H^*} = -0.86$ V on In(101)

The reaction barrier of surface hydrogenation reactions are performed using the climbing image nudged elastic band method (CI-NEB),¹² and vibrational frequencies were evaluated to confirm minima and transition states. As listed in **Table S4**, we calculated reaction barriers via surface hydrogenation mechanism at two different potentials, named as U_{H^*} and U_{SHE} . The former one U_{H^*} refers to the potential at which

$\Delta G_{H^*} = 0$ and the activation energies are directly calculated by CI-NEB method. The later one U_{SHE} is defined as $U = 0$ V vs. SHE. On the basis of framework of Janik et al,¹³⁻¹⁴ the reaction barriers at U_{SHE} are extrapolated from U_{H^*} by Butler-Volmer kinetics with a symmetry factor of 0.5. Therefore, the reaction barriers calculated by transition state theory and Marcus theory can be compared at the same electrode potential.

Table S5. The Structures of initial state (IS), transition state (TS), and final state (FS) for CO₂ reduction to CO and FA on Cu(111), Au(111), and In(101) surfaces.

Substrates	CO ₂ * + H* → COOH*		
	IS	TS	FS
Cu(111)			
Au(111)			
In(101)			
Substrates	CO ₂ * + H* → HCOO*		
	IS	TS	FS
Cu(111)			
Au(111)			
In(101)			
Substrates	COOH* + H* → CO* + H ₂ O		
	IS	TS	FS
Cu(111)			
Au(111)			
In(101)			
Substrates	HCOO* + H* → HCOOH*		
	IS	TS	FS
Cu(111)			

Au(111)			
In(101)			

The calculated reaction barriers of surface hydrogenation reaction by CI-NEB method are quite close to those of proton-coupled electron transfer reaction by Marcus theory for Cu(111) and Au(111) surfaces. However, the calculated reaction barriers of hydrogenation of CO_2^* to HCOO^* on In(101) surface by CI-NEB method are suspicious. The abnormal activation energy values on In(101) surface calculated by CI-NEB method can be attributed to that the formation of surface H^* is quite difficult ($\Delta G = 0.86 \text{ eV}$) and the hydrogenation of CO_2^* to HCOO^* is highly spontaneous ($\Delta G = -1.25 \text{ eV}$). In other words, there is a huge gap between the onset potential of hydrogen formation and the onset potential of hydrogen transfer. Based on the CI-NEB calculation results, the rate-determining step for FA formation on In(101) surface should be the second electron transfer step, which give a Tafel slope around 40 mV. It is obviously inconsistent with experimental values around 120 mV.

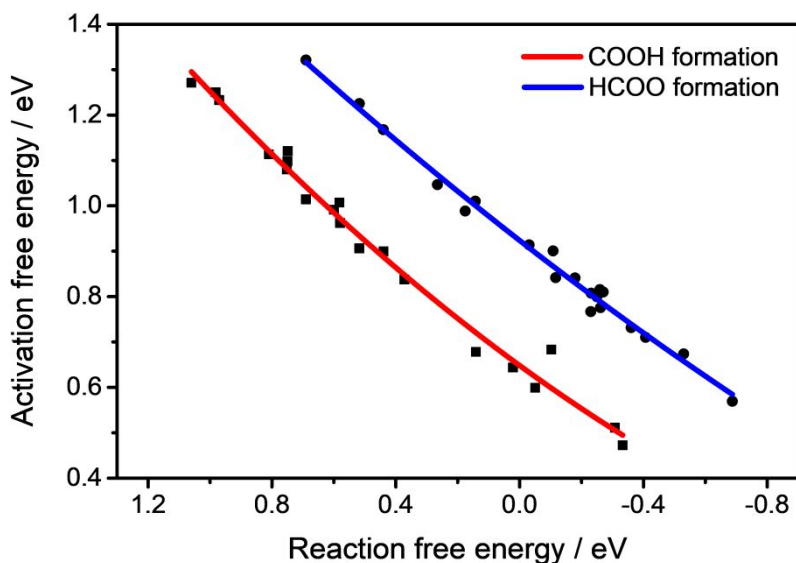


Figure S1. BEP relations between activation free energies and reaction free energies for competing COOH and HCOO formations on various metal surfaces.

Figure S1 shows that the reaction barriers of both COOH* and HCOO* formations decrease as the increasing of reaction driving force ($-\Delta G$) with similar scaling relations (slope of E_a vs. ΔG). However, the reaction barriers of COOH* formations are generally about 0.3 eV lower than that of HCOO* formation for the same ΔG value. This further demonstrate the CO formation through COOH* pathway is kinetics-controlled. Since the BEP relations of competing COOH and HCOO formations are quite different, bare thermodynamic calculations of ΔG without considering the reaction barrier are insufficient to estimate the catalytic activity and selectivity.

Table S6. Reaction Gibbs free energies (eV) of two-electron-two-proton reduction of CO₂ on various metal surfaces.

Surfaces	1a ^a	1b ^b	2a ^c	2b ^d
Cu(100)	0.37	-0.36	-0.59	0.50
Cu(110)	0.14	-0.69	-0.51	0.64
Cu(111)	0.60	-0.03	-0.80	0.26
Ag(100)	0.75	-0.12	-0.54	0.33
Ag(110)	0.52	-0.41	-0.31	0.65
Ag(111)	0.98	0.18	-0.62	0.14
Au(100)	0.58	0.52	-0.60	-0.25
Au(110)	0.44	0.14	-0.60	0.02
Au(111)	0.75	0.69	-0.51	-0.38
Zn(001)	0.78	-0.18	-0.25	0.47
Cd(001)	0.75	-0.26	-0.28	0.53
In(101)	0.91	-0.32	-0.45	0.58
Tl(001)	1.06	-0.23	-0.61	0.47
Sn(100)	0.58	-0.27	-0.40	0.30
Pb(111)	0.97	-0.02	-0.48	0.34
Ni(111)	-0.05	-0.23	-1.30	0.27
Pd(111)	0.02	0.27	-1.52	-0.14
Pt(111)	-0.10	0.44	-1.05	-0.30
Rh(111)	-0.33	-0.26	-0.99	0.23
Ir(111)	-0.31	-0.11	-1.03	0.18

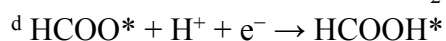
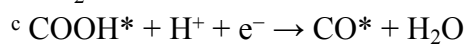
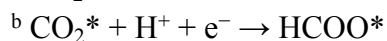
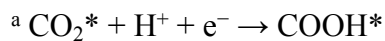
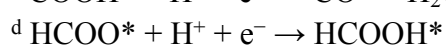
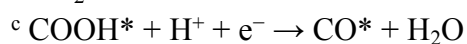
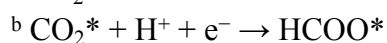
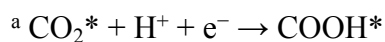


Table S7. Reorganization energies (eV) of two-electron-two-proton reduction of CO₂ on various metal surfaces.

Surfaces	1a ^a		1b ^b		2a ^c		2b ^d	
	λ_R	λ_P	λ_R	λ_P	λ_R	λ_P	λ_R	λ_P
Cu(100)	2.18	2.69	2.37	5.52	3.41	2.66	1.66	1.53
Cu(110)	1.86	2.58	2.04	5.64	3.40	2.53	1.50	1.46
Cu(111)	2.45	2.89	2.60	5.70	3.46	2.82	1.90	1.60
Ag(100)	2.53	2.73	2.50	5.44	3.25	2.76	1.78	1.56
Ag(110)	2.22	2.98	2.24	5.85	3.40	2.37	1.82	1.50
Ag(111)	2.77	2.49	2.64	5.70	3.46	2.61	1.91	1.63
Au(100)	2.65	2.73	2.97	5.53	3.71	2.56	1.89	1.72
Au(110)	2.39	3.08	2.75	5.59	3.96	2.15	1.92	1.58
Au(111)	2.81	2.74	3.05	5.40	3.72	2.20	1.95	1.78
Zn(001)	2.46	2.84	2.49	5.81	3.56	2.45	1.99	1.89
Cd(001)	2.59	2.87	2.36	5.70	2.74	2.77	1.86	1.76
In(101)	2.37	2.71	2.29	5.75	2.94	2.91	1.92	1.96
Tl(001)	2.37	2.44	2.31	5.55	2.44	3.18	1.61	1.75
Sn(100)	2.34	2.95	2.54	5.70	3.32	2.63	2.01	2.05
Pb(111)	2.68	2.54	2.49	5.59	2.87	2.91	1.80	1.86
Ni(111)	1.80	3.62	2.48	5.64	3.17	3.32	2.00	1.49
Pd(111)	1.91	3.54	2.77	5.26	3.03	3.05	1.88	1.59
Pt(111)	2.37	3.66	2.99	5.18	3.12	2.54	1.91	1.68
Rh(111)	1.59	3.90	2.49	5.89	3.46	2.82	2.01	1.47
Ir(111)	1.73	3.92	2.68	5.70	3.58	2.58	2.09	1.54



4. Potential energy curves

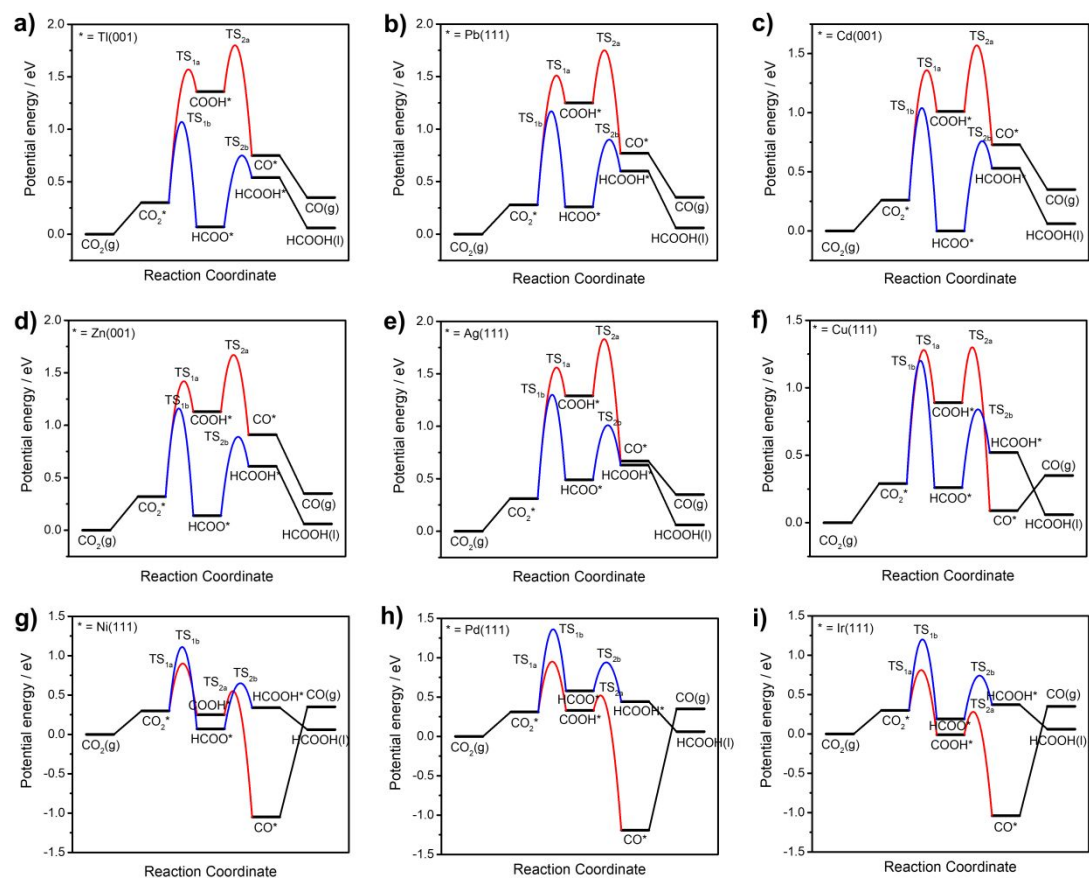


Figure S2. Potential energy curves of two-electron-two-proton reduction of CO_2 on (a) $\text{Ti}(001)$, (b) $\text{Pb}(111)$, (c) $\text{Cd}(001)$, (d) $\text{Zn}(001)$, (e) $\text{Ag}(111)$, (f) $\text{Cu}(111)$, (g) $\text{Ni}(111)$, (h) $\text{Pd}(111)$, and (i) $\text{Ir}(111)$ surfaces at $U = 0$ V vs. SHE.

5. Activation barriers and rate constants

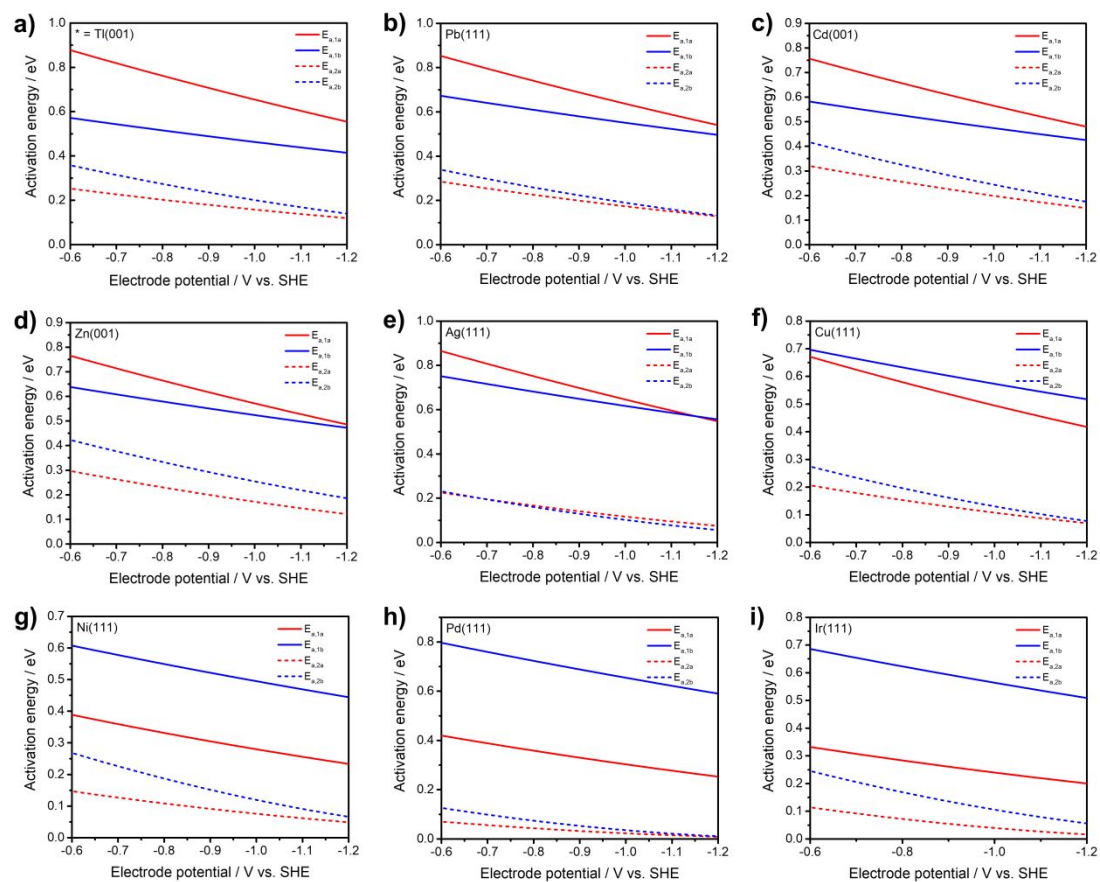


Figure S3. Potential-dependent activation barriers of two-electron-two-proton reduction of CO_2 on (a) Tl(001), (b) Pb(111), (c) Cd(001), (d) Zn(001), (e) Ag(111), (f) Cu(111), (g) Ni(111), (h) Pd(111), and (i) Ir(111) surfaces.

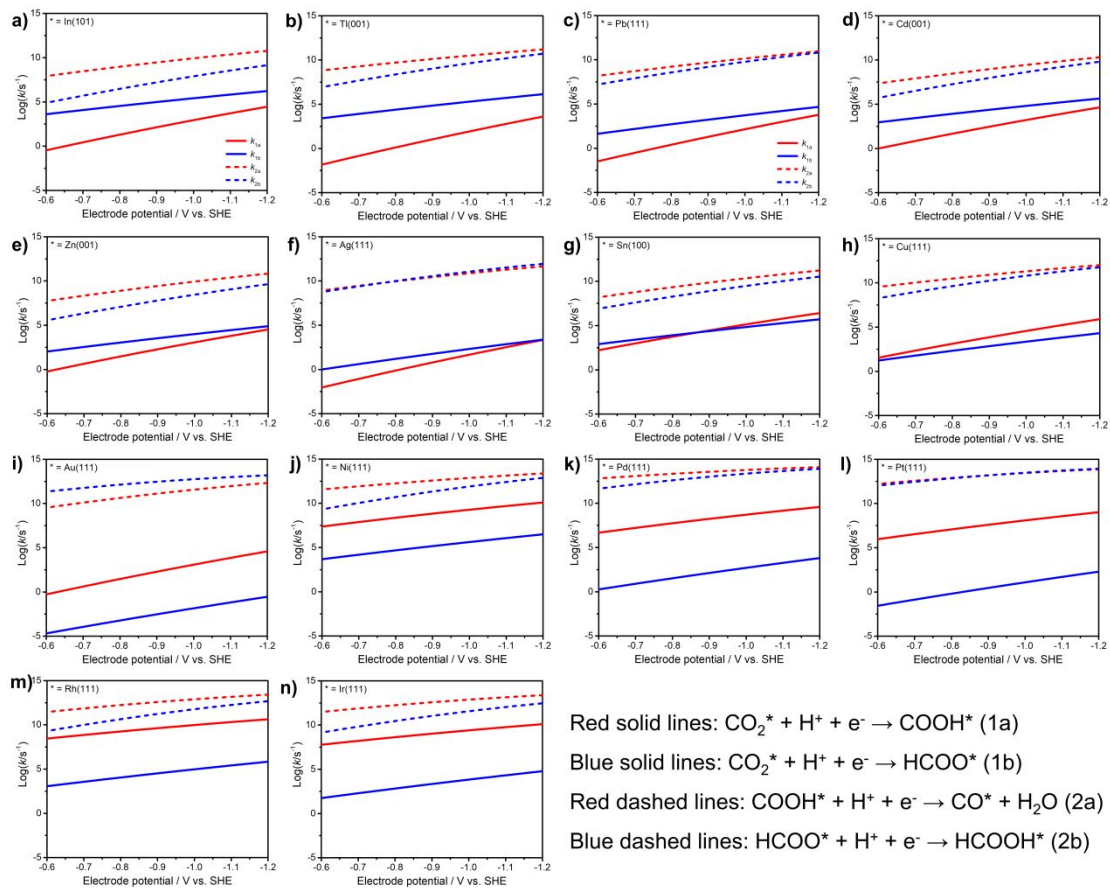


Figure S4. Potential-dependent Marcus-Gerischer rate constant of two-electron-two-proton reduction of CO_2 on (a) In (101) (b) Tl(001), (c) Pb(111), (d) Cd(001), (e) Zn(001), (f) Ag(111), (g) Sn(100), (h) Cu(111), (i) Au(111), (j) Ni(111), (k) Pd(111), (l) Pt(111), (m) Rh(111), and (n) Ir(111) surfaces.

Table S8. Fitted reaction activation barriers (in eV) and symmetry factors (dimensionless) for HCOO* and COOH* formation as a function of electrode potential U (in V vs. SHE).

Surface	$\text{CO}_2^* \rightarrow \text{HCOO}^*$		$\text{CO}_2^* \rightarrow \text{COOH}^*$	
	E_a	β	E_a	β
Cu(100)	$0.05U^2+0.34U+0.73$	$0.10U+0.34$	$0.09U^2+0.52U+0.84$	$0.18U+0.52$
Cu(110)	$0.04U^2+0.28U+0.57$	$0.08U+0.28$	$0.08U^2+0.44U+0.68$	$0.16U+0.68$
Cu(111)	$0.05U^2+0.39U+0.91$	$0.10U+0.39$	$0.09U^2+0.59U+0.99$	$0.18U+0.59$
Ag(100)	$0.05U^2+0.38U+0.84$	$0.10U+0.38$	$0.10U^2+0.63U+1.08$	$0.20U+0.63$
Ag(110)	$0.05U^2+0.32U+0.71$	$0.10U+0.32$	$0.09U^2+0.56U+0.91$	$0.18U+0.56$
Ag(111)	$0.06U^2+0.43U+0.99$	$0.10U+0.32$	$0.09U^2+0.70U+1.25$	$0.18U+0.70$
Au(100)	$0.06U^2+0.48U+1.22$	$0.12U+0.48$	$0.09U^2+0.59U+1.01$	$0.18U+0.59$
Au(110)	$0.05U^2+0.42U+1.01$	$0.10U+0.42$	$0.09U^2+0.55U+0.90$	$0.18U+0.55$
Au(111)	$0.06U^2+0.51U+1.32$	$0.12U+0.51$	$0.09U^2+0.64U+1.12$	$0.18U+0.64$
Zn(001)	$0.05U^2+0.37U+0.84$	$0.10U+0.37$	$0.10U^2+0.64U+1.13$	$0.20U+0.64$
Cd(001)	$0.05U^2+0.35U+0.77$	$0.10U+0.35$	$0.09U^2+0.63U+1.10$	$0.20U+0.63$
In(101)	$0.05U^2+0.34U+0.74$	$0.10U+0.34$	$0.10U^2+0.67U+1.16$	$0.20U+0.67$
Tl(001)	$0.05U^2+0.35U+0.77$	$0.10U+0.35$	$0.10U^2+0.72U+1.27$	$0.20U+0.72$
Sn(100)	$0.05U^2+0.36U+0.81$	$0.10U+0.36$	$0.09U^2+0.58U+0.96$	$0.18U+0.58$
Pb(111)	$0.05U^2+0.39U+0.89$	$0.10U+0.39$	$0.10U^2+0.69U+1.23$	$0.20U+0.69$
Ni(111)	$0.05U^2+0.36U+0.81$	$0.10U+0.36$	$0.07U^2+0.39U+0.60$	$0.14U+0.39$
Pd(111)	$0.06U^2+0.45U+1.05$	$0.12U+0.45$	$0.08U^2+0.42U+0.64$	$0.16U+0.42$
Pt(111)	$0.06U^2+0.48U+1.17$	$0.12U+0.48$	$0.07U^2+0.42U+0.68$	$0.14U+0.42$
Rh(111)	$0.05U^2+0.34U+0.81$	$0.12U+0.34$	$0.06U^2+0.32U+0.47$	$0.12U+0.32$
Ir(111)	$0.05U^2+0.39U+0.90$	$0.10U+0.39$	$0.06U^2+0.33U+0.51$	$0.12U+0.33$

The rate-determining step (RDS) approximation was used to derive the apparent charge transfer coefficient and Tafel slope. As seen from **Figure S4**, the calculated rate constant of the second electron transfer steps (dashed lines) are much larger than that of the first electron transfer steps (solid lines). Thus, we conclude that the RDS steps for CO₂ reduction to CO and FA are 1a and 1b, respectively. Under RDS approximation, the

current density can be expressed as follow,

$$j = 2Fk(U)\theta_{\text{CO}_2^*}(U)a_{\text{H}^+}(\text{pH})$$
$$= 2Fk^0 \exp\left(-\frac{(n' + \beta_{\text{RDS}})F\eta}{k_B T}\right)\theta_{\text{CO}_2^*}(U)a_{\text{H}^+}(\text{pH})$$

where n' is the number of electrons transferred before RDS and β_{RDS} is the symmetry factor of RDS. For CO_2 reduction to FA and CO, n' is zero since the RDS is the first electron transfer step. So, the apparent charge transfer coefficient equals to β . In addition, the competing CO_2 reductions to CO and FA share the same reactants, the coverage (concentration) effect can be ignored for the same experimental conditions.

6. Faradaic efficiencies

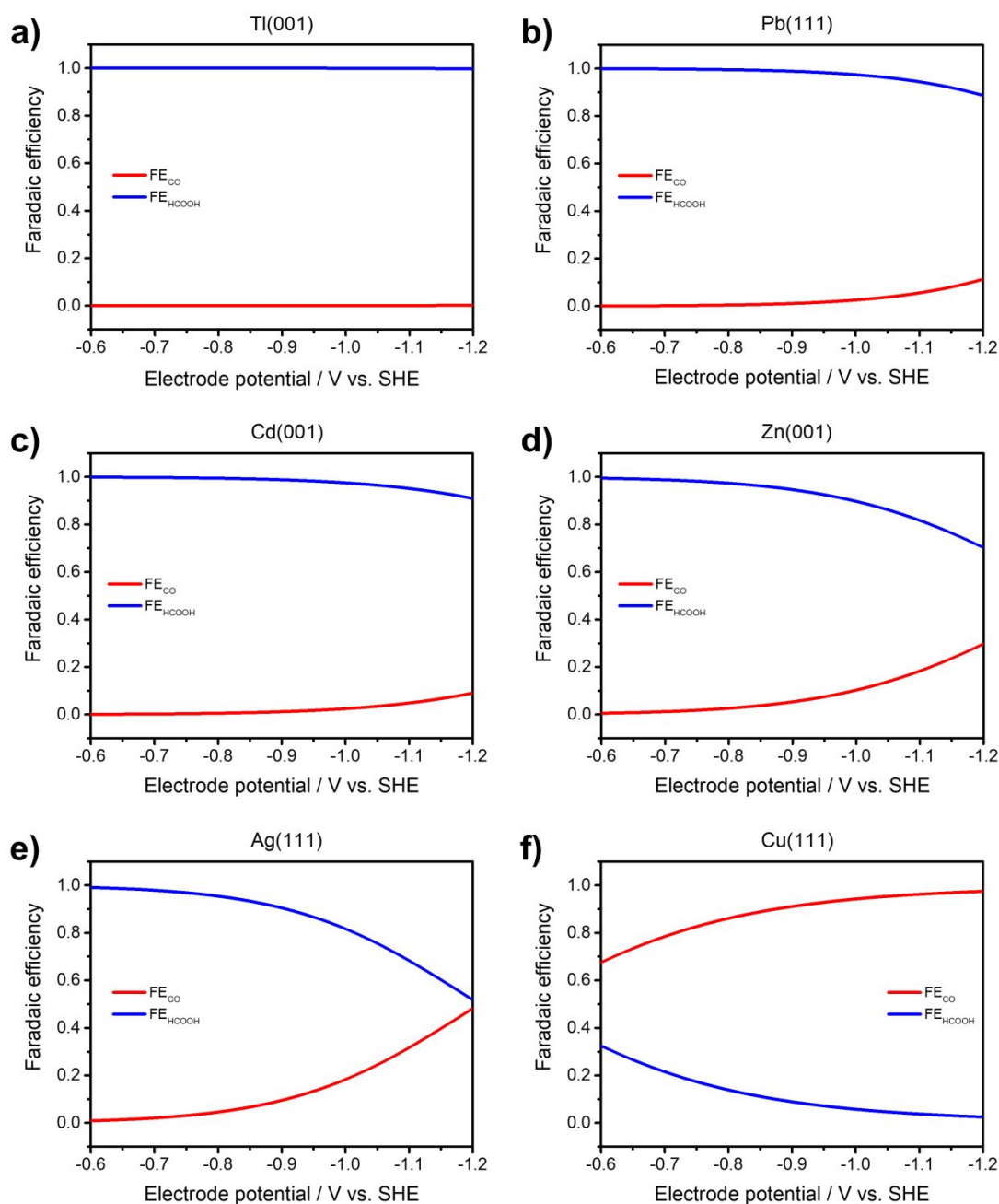


Figure S5. Potential-dependent Faradaic efficiencies of electrochemical reduction of CO₂ to CO and HCOOH on (a) Ti(001), (b) Pb(111), (c) Cd(001), (d) Zn(001), (e) Ag(111), and (f) Cu(111) surfaces.

The computational results well explain the large gap between lower limit and upper limit FE measured on Zn and Cd electrodes.¹⁵ It is worse noting that the calculated FE_{CO} on Ag single crystal facets, particularly under low reduction potential,¹⁶ are obviously lower than experimental value measured on Ag electrode or nanostructures,

which were considered as one of the best catalyst to reduce CO_2 to CO .¹⁷⁻¹⁹ Experimentally, the CO_2 reduction on silver single crystal surfaces exhibit very negative onset potential,²⁰⁻²¹ which is supported by our calculations shown in **Figure S2**. At $U = -1.2$ V vs. SHE, the computed FE_{CO} are 0.48 on Ag(111), 0.47 on Ag(100), and 0.62 on Ag(110). These values are comparable with experimental results measured on silver single crystal surfaces, in which the measured CO Faradaic efficiency increases in an order of $\text{Ag}(110) > \text{Ag}(111) \approx \text{Ag}(100)$.²¹ In addition, computation results by Liu et al.²²⁻²³ demonstrated the onset potential of CO formation on silver can be further lowered on more active sites such as Ag(211).

7. Hydrogen evolution reaction

DFT calculations on HER were carried out using both Perdew-Burke-Ernzerhof (PBE)²⁴ and revised PBE (RPBE)²⁵ exchange-correlation functionals. The overall HER pathway includes two steps: adsorption of hydrogen on the catalyst (H^*) from initial state ($H^+ + e^- + *$), and release of molecular hydrogen ($1/2H_2 + *$), where $*$ denotes the catalyst.

The Gibbs free-energy of the adsorption of atomic hydrogen ($\Delta G_{H^*}^0$) under standard condition ($pH = 0$) is obtained by Eq (13)

$$\Delta G_{H^*}^0 = \Delta E_H + \Delta E_{ZPE} + T\Delta S_H \quad (13)$$

Where, ΔE_{ZPE} , and ΔS_H are the difference in zero-point energy, and entropy between hydrogen adsorption and hydrogen in the gas phase, respectively. By neglecting the contributions from the catalysts to both ΔE_{ZPE} and ΔS_H , Eq (14) can be rewritten as²⁶

$$\Delta G_{H^*}^0 = \Delta E_H + 0.24 \text{ eV} \quad (14)$$

ΔE_H is the differential hydrogen adsorption energy, which is defined by Eq (15):

$$\Delta E_H = E_{H^*} - E_* - \frac{1}{2}E_{H_2} \quad (15)$$

In this work, the same theoretical model was used to treat both CO₂RR and HER and compare reaction kinetics. Concerted proton and electron transfer mechanism was adopted.



For CO₂RR, A is CO₂. For HER, A is H₂O for Volmer reaction and A is H for Heyrovsky reaction. The HER on these metals are assumed to adopt Volmer-Heyrovsky mechanism and the potential-dependent reaction barriers of two proton-coupled electron transfer steps are calculated using similar theoretical framework for CO₂RR.

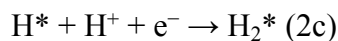
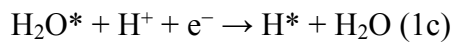


Table S9. Calculated ΔE_{H} and ΔG_{H} (in eV) on various metal surfaces by PBE functional and RPBE functional.

Surface	PBE		RPBE	
	ΔE_{H}	ΔG_{H}	ΔE_{H}	ΔG_{H}
Cu(111)	-0.14	0.10	-0.03	0.21
Ag(111)	0.27	0.51	0.39	0.63
Au(111)	0.25	0.49	0.39	0.63
Zn(001)	0.71	0.95	0.58	0.82
Cd(001)	0.60	0.84	0.62	0.86
In(101)	0.62	0.86	0.54	0.78
Tl(001)	0.74	0.98	0.78	1.02
Sn(100)	0.31	0.55	0.38	0.62
Pb(111)	0.65	0.89	0.78	1.02
Ni(111)	-0.66	-0.42	-0.52	-0.28
Pd(111)	-0.63	-0.39	-0.49	-0.25
Pt(111)	-0.48	-0.24	-0.33	-0.09
Rh(111)	-0.52	-0.28	-0.37	-0.13
Ir(111)	-0.36	-0.12	-0.22	0.02

DFT calculations on HER were carried out by both PBE and RPBE functional. The computed ΔE_{H} and ΔG_{H} on different metal surfaces are shown in **Table S7**. In general, the calculated hydrogen adsorption energy by RPBE functional is about 0.1 eV higher than PBE functional. Specifically, the calculated ΔG_{H} on Pt(111) surface by RPBE (-0.09 eV) is closer to 0 than by PBE (-0.24 eV), which agrees with previous report.²⁷ However, in order to maintain consistency in the computational method, the kinetic properties of HER are studied by using the same PBE functional as CO₂RR simulations.

Table S10. Reorganization energies (in eV) of HER on various metal surfaces.

$\text{H}_2\text{O}^* + \text{H}^+ + \text{e}^- \rightarrow \text{H}^* + \text{H}_2\text{O} \text{ (1c)}$								
Surface	$\lambda_{\text{R}}^{\text{o,ET}}$	$\lambda_{\text{P}}^{\text{o,ET}}$	$\lambda_{\text{R}}^{\text{O,PT}}$	$\lambda_{\text{P}}^{\text{O,PT}}$	$\lambda_{\text{R}}^{\text{i}}$	$\lambda_{\text{P}}^{\text{i}}$	λ_{R}	λ_{P}
Cu(111)	1.37	1.65	0.06	0.11	1.64	2.60	3.08	4.36
Ag(111)	1.37	1.65	0.06	0.11	1.61	1.77	3.05	3.53
Au(111)	1.37	1.65	0.06	0.11	2.53	2.34	3.97	4.10
Zn(001)	1.37	1.65	0.06	0.11	1.01	1.50	2.45	3.26
Cd(001)	1.37	1.65	0.06	0.11	0.83	1.55	2.27	3.30
In(101)	1.37	1.65	0.06	0.11	0.83	1.10	2.27	2.86
Tl(001)	1.37	1.65	0.06	0.11	1.44	0.80	2.88	2.56
Sn(100)	1.37	1.65	0.06	0.11	1.80	1.46	3.24	3.22
Pb(111)	1.37	1.65	0.06	0.11	1.82	1.63	3.26	3.38

$\text{H}^* + \text{H}^+ + \text{e}^- \rightarrow \text{H}_2^* \text{ (2c)}$								
Surface	$\lambda_{\text{R}}^{\text{o,ET}}$	$\lambda_{\text{P}}^{\text{o,ET}}$	$\lambda_{\text{R}}^{\text{O,PT}}$	$\lambda_{\text{P}}^{\text{O,PT}}$	$\lambda_{\text{R}}^{\text{i}}$	$\lambda_{\text{P}}^{\text{i}}$	λ_{R}	λ_{P}
Cu(111)	1.65	1.51	0.11	0.09	2.49	0.99	4.25	2.59
Ag(111)	1.65	1.51	0.11	0.09	2.00	1.19	3.75	2.78
Au(111)	1.65	1.51	0.11	0.09	2.19	1.59	3.95	3.19
Zn(001)	1.65	1.51	0.11	0.09	1.55	0.82	3.31	2.42
Cd(001)	1.65	1.51	0.11	0.09	1.30	0.70	3.06	2.30
In(101)	1.65	1.51	0.11	0.09	1.19	0.77	2.94	2.37
Tl(001)	1.65	1.51	0.11	0.09	0.92	1.23	2.67	2.83
Sn(100)	1.65	1.51	0.11	0.09	1.74	1.56	3.50	3.16
Pb(111)	1.65	1.51	0.11	0.09	1.40	1.44	3.16	3.03

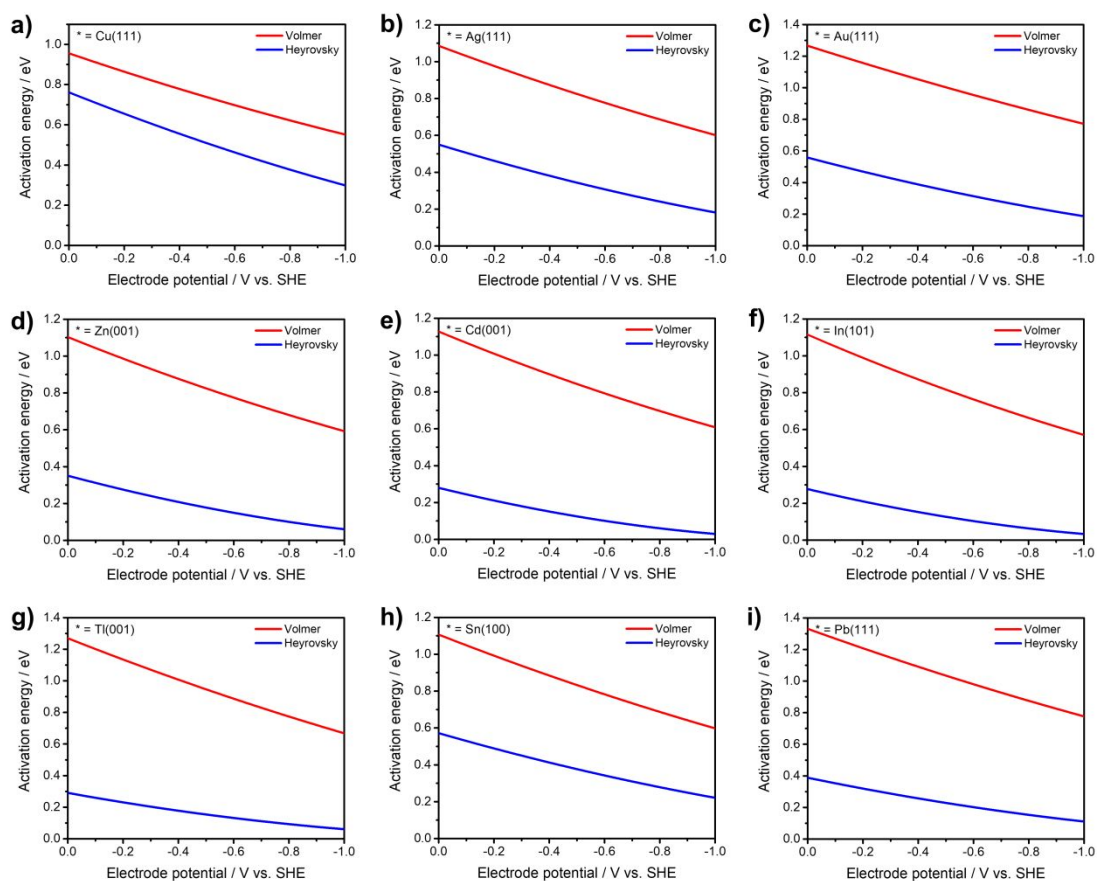


Figure S6. Potential-dependent activation barriers of Volmer reaction and Heyrovsky reaction on (a) Cu(111), (b) Ag(111), (c) Au(111), (d) Zn(001), (e) Cd(001), (f) In(101), (g) Tl(001), (h) Sn(100), and (i) Pb(111) surfaces.

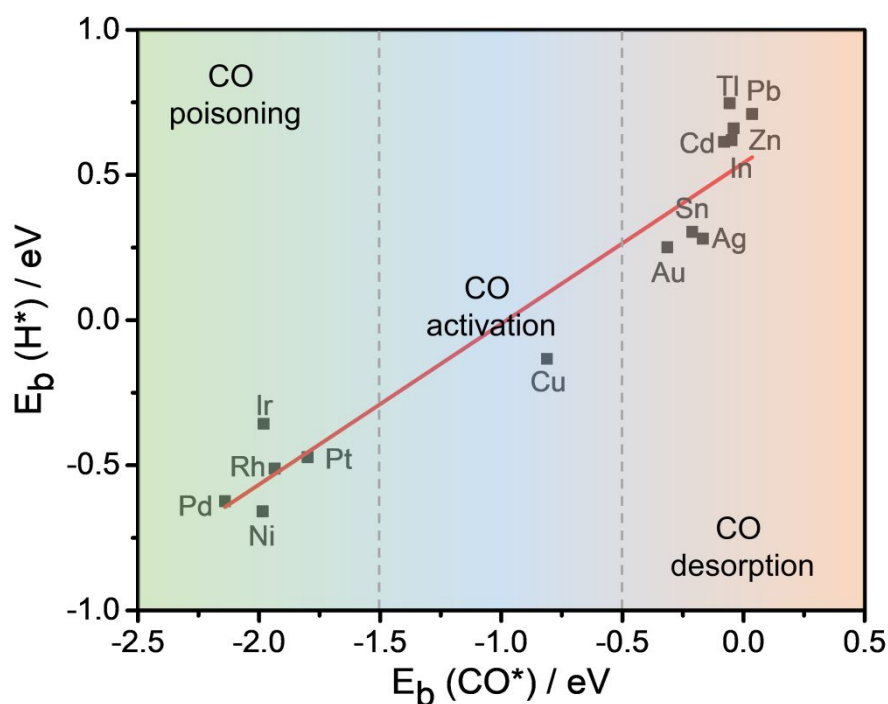


Figure S7. Scaling relation of binding energies of CO^* and H^* adsorbed on various metal surfaces.

The binding energies of CO^* show almost linear relation with the binding energies of H^* . It is therefore we can use to binding energy of CO to estimate the binding strength of H^* and therefore the HER activity. As seen from **Figure S5**, the studied metal catalysts are divided into three regions. P-block metals and Ds-block metals except Cu fall into CO desorption region, where the HER activity is also very weak duo to weak H^* binding energy. Transition metals falls into CO poisoning region, where the CO hydrogenations take places extremely non-spontaneously as shown in **Figure 8c** while HER show high activity as shown in **Figure 8b**. Cu with neither too strong nor too weak CO binding strength is the unique metal located at the CO activation region. Meanwhile the HER side reactions are unavoidable, which becomes a main drawback of Cu-based CO_2RR catalysts.

8. References

- (1) Marcus, R. A. On the Theory of Oxidation-Reduction Reactions Involving Electron Transfer. I. *J. Chem. Phys.* **1956**, 24 (5), 966-978.
- (2) Marcus, R. A. Electron transfer reactions in chemistry theory and experiment. *J. Electroanal. Chem.* **1997**, 438 (1-2), 251-259.
- (3) Gao, S.-T.; Xiang, S.-Q.; Shi, J.-L.; Zhang, W.; Zhao, L.-B. Theoretical Understanding of the Electrochemical Reaction Barrier: A Kinetic Study of CO₂ Reduction Reaction on Copper Electrodes. *Phys. Chem. Chem. Phys.* **2020**, 22 (17), 9607-9615.
- (4) Xiang, S.-Q.; Gao, S.-T.; Shi, J.-L.; Zhang, W.; Zhao, L.-B. Developing microkinetic model for electrocatalytic reduction of carbon dioxide on copper electrode. *J. Catal.* **2021**, 393, 11-19.
- (5) Xiang, S.-Q.; Shi, J.-L.; Gao, S.-T.; Zhang, W.; Zhao, L.-B. Thermodynamic and Kinetic Competition between C–H and O–H Bond Formation Pathways during Electrochemical Reduction of CO on Copper Electrodes. *ACS Catal.* **2021**, 11 (4), 2422-2434.
- (6) Costentin, C.; Evans, D. H.; Robert, M.; Savéant, J.-M.; Singh, P. S. Electrochemical Approach to Concerted Proton and Electron Transfers. Reduction of the Water–Superoxide Ion Complex. *J. Am. Chem. Soc.* **2005**, 127 (36), 12490-12491.
- (7) Costentin, C.; Robert, M.; Savéant, J.-M. Electrochemical and Homogeneous Proton-Coupled Electron Transfers: Concerted Pathways in the One-Electron Oxidation of a Phenol Coupled with an Intramolecular Amine-Driven Proton Transfer. *J. Am. Chem. Soc.* **2006**, 128 (14), 4552-4553.
- (8) Mishra, A. K.; Waldeck, D. H. A Unified Model for the Electrochemical Rate Constant That Incorporates Solvent Dynamics. *J. Phys. Chem. C* **2009**, 113 (41), 17904-17914.
- (9) Zhao, L.-B.; Mishra, A. K.; Waldeck, D. H. Voltammetry Can Reveal Differences between the Potential Energy Curve (pec) and Density of States (dos) Models for Heterogeneous Electron Transfer. *J. Phys. Chem. C* **2013**, 117 (40), 20746-20761.
- (10) Mishra, A. K.; Bhattacharjee, B.; Rangarajan, S. K. Theory of electron transfer processes via chemisorbed intermediates: Part II. Current-potential characteristics. *J. Electroanal. Chem.* **1992**, 331 (1–2), 801-813.
- (11) Krishtalik, L. I. The mechanism of an elementary act of proton transfer in homogeneous and electrode reactions. *J. Electroanal. Chem.* **1979**, 100 (1), 547-561.
- (12) Henkelman, G.; Uberuaga, B. P.; Jónsson, H. A climbing image nudged elastic band method for finding saddle points and minimum energy paths. *J. Chem. Phys.* **2000**, 113 (22), 9901-9904.
- (13) Nie, X.; Esopi, M. R.; Janik, M. J.; Asthagiri, A. Selectivity of CO₂ Reduction on Copper Electrodes: The Role of the Kinetics of Elementary Steps. *Angew. Chem., Int. Ed.* **2013**, 52 (9), 2459-2462.
- (14) Luo, W.; Nie, X.; Janik, M. J.; Asthagiri, A. Facet Dependence of CO₂ Reduction Paths on Cu Electrodes. *ACS Catal.* **2016**, 6 (1), 219-229.
- (15) Hori, Y.; Kikuchi, K.; Suzuki, S. Production of CO and CH₄ in electrochemical

reduction of CO₂ at metal electrodes in aqueous hydrogencarbonate solution. *Chem. Lett.* **1985**, 14 (11), 1695-1698.

(16) Bohra, D.; Ledezma-Yanez, I.; Li, G.; de Jong, W.; Pidko, E. A.; Smith, W. A. Lateral Adsorbate Interactions Inhibit HCOO⁻ while Promoting CO Selectivity for CO₂ Electrocatalysis on Silver. *Angew. Chem., Int. Ed.* **2019**, 58 (5), 1345-1349.

(17) Wang, G.; Chen, J.; Ding, Y.; Cai, P.; Yi, L.; Li, Y.; Tu, C.; Hou, Y.; Wen, Z.; Dai, L. Electrocatalysis for CO₂ conversion: from fundamentals to value-added products. *Chem. Soc. Rev.* **2021**, 50, 4993-5061.

(18) Singh, M. R.; Kwon, Y.; Lum, Y.; Ager, J. W.; Bell, A. T. Hydrolysis of Electrolyte Cations Enhances the Electrochemical Reduction of CO₂ over Ag and Cu. *J. Am. Chem. Soc.* **2016**, 138 (39), 13006-13012.

(19) Ma, M.; Trzeźniewski, B. J.; Xie, J.; Smith, W. A. Selective and Efficient Reduction of Carbon Dioxide to Carbon Monoxide on Oxide-Derived Nanostructured Silver Electrocatalysts. *Angew. Chem., Int. Ed.* **2016**, 55 (33), 9748-9752.

(20) Hoshi, N.; Kato, M.; Hori, Y. Electrochemical reduction of CO₂ on single crystal electrodes of silver Ag(111), Ag(100) and Ag(110). *J. Electroanal. Chem.* **1997**, 440 (1), 283-286.

(21) Clark, E. L.; Ringe, S.; Tang, M.; Walton, A.; Hahn, C.; Jaramillo, T. F.; Chan, K.; Bell, A. T. Influence of Atomic Surface Structure on the Activity of Ag for the Electrochemical Reduction of CO₂ to CO. *ACS Catal.* **2019**, 9 (5), 4006-4014.

(22) Liu, S.; Sun, C.; Xiao, J.; Luo, J.-L. Unraveling Structure Sensitivity in CO₂ Electroreduction to Near-Unity CO on Silver Nanocubes. *ACS Catal.* **2020**, 10 (5), 3158-3163.

(23) Qi, K.; Zhang, Y.; Li, J.; Charmette, C.; Ramonda, M.; Cui, X.; Wang, Y.; Zhang, Y.; Wu, H.; Wang, W., et al. Enhancing the CO₂-to-CO Conversion from 2D Silver Nanoprism via Superstructure Assembly. *ACS Nano* **2021**, 15 (4), 7682-7693.

(24) Perdew, J. P.; Burke, K.; Ernzerhof, M. Generalized Gradient Approximation Made Simple. *Phys. Rev. Lett.* **1996**, 77 (18), 3865-3868.

(25) Zhang, Y.; Yang, W. Comment on "Generalized Gradient Approximation Made Simple". *Phys. Rev. Lett.* **1998**, 80 (4), 890-890.

(26) Zhang, L.; Jia, Y.; Gao, G.; Yan, X.; Chen, N.; Chen, J.; Soo, M. T.; Wood, B.; Yang, D.; Du, A., et al. Graphene Defects Trap Atomic Ni Species for Hydrogen and Oxygen Evolution Reactions. *Chem* **2018**, 4 (2), 285-297.

(27) Nørskov, J. K.; Bligaard, T.; Logadottir, A.; Kitchin, J. R.; Chen, J. G.; Pandelov, S.; Stimming, U. Trends in the Exchange Current for Hydrogen Evolution. *J. Electrochem. Soc.* **2005**, 152 (3), J23.